

Quantitative measures of image resolution for seismic survey design

Richard L. Gibson, Jr.,* and Constantinos Tzimeas*

ABSTRACT

Illumination and fold analyses can provide valuable information for the design of seismic surveys, but generally they do not provide quantitative results that are directly related to the seismic images that would be obtained using a proposed acquisition geometry. On the other hand, the Beylkin (1985) equation predicts the spatial resolution of prestack migration using the acquisition geometry and an earth model, providing a simple yet effective tool for survey design. Calculations for a simple homogeneous earth model demonstrate the advantages of this approach. Specifically, the variations in spatial resolution within the model show that the best resolution results from singlefold, zero-offset experiments for very

simple acquisition geometries. Applications of the same design method to a realistic salt model show that some results are not surprising, such as decreases in resolution beneath the salt structure. However, the best resolution beneath the salt is obtained with the maximum offset for a trial single-cable marine geometry, not the zero-offset source–receiver pairs. This is a consequence of ray bending by the salt structure and the geometry of the acquisition lines. The result clearly demonstrates the utility of the proposed survey design tool. We also find that a land circular source/radial receiver line array design shows strong potential for improved resolution over the simple marine geometry. Furthermore, tests show that the land survey should display more robust results as the S/N ratio decreases.

INTRODUCTION

Seismic survey design must take into account many different factors, including economic considerations as well as practical constraints such as those introduced by features such as lakes or rivers on land or drilling platforms in marine settings. One of the most important issues is clearly to adjust the acquisition geometry to optimize the seismic images of the target reservoir formations. For example, Maldonado and Hussein (1994) suggest that a concentric circle source–receiver layout may produce better images near salt domes than some simpler designs. Conventional seismic survey design procedures tend to apply simple, qualitative analyses to compare these various competing survey designs or to assess variations of image quality for a specific survey. The simplest procedure is to compute fold using the source–receiver geometry, completely neglecting earth structure and wave propagation effects. A better approach is that proposed by Slawson et al. (1994; see also Slawson et al., 1995), who suggest a model-based 3-D acquisition design to incorporate structural complexities and velocity variations into

an accurate common reflection point (CRP) binning analysis for a more realistic representation of the imaging capabilities of the proposed acquisition geometry. This method can easily identify regions of poor or no CRP bin coverage, thus facilitating the modification and subsequent improvement of the acquisition survey design under examination. However, because the CRP coverage analysis only counts the total number of ray reflection points at a specific location, it neglects any information associated with the directions of the raypaths at the image point.

Therefore, these procedures do not directly produce information that can be used for quantitative analyses of spatial resolution of the seismic surveys. Beylkin (1984; 1985) has made an important contribution to this field of study by demonstrating that the spatial resolution of seismic imaging depends directly on the propagation directions of the raypaths from source and receiver at an imaging point of interest. A survey design utilizing this result, which quantitatively predicts spatial resolution, has a distinct advantage over more conventional illumination methods because it has a rigorous, theoretical foundation

Manuscript received by the Editor November 6, 2000; revised manuscript received October 10, 2001.

*Texas A&M University, Department of Geology and Geophysics, MS 3115, College Station, Texas 77843-3115. E-mail: gibson@geo.tamu.edu; costas@nyssa.tamu.edu.

© 2002 Society of Exploration Geophysicists. All rights reserved.

on the inversion based on the generalized Radon transform (GRT) (Beylkin, 1985; Beylkin and Burrige, 1990). Miller et al. (1989) and von Seggern (1991) utilize this result to examine the influence of survey geometry on imaging results, although they do not emphasize the implications for survey design. More recently, von Seggern (1994) considered the influence of 3-D acquisition geometry on horizontal image resolution, suggesting that the survey design would have minimal impact on the final result. However, Vermeer (1999) points out that this is likely an artifact of the coarse measurement analysis and of sorting the source–receiver pairs in the calculations.

In this paper, we briefly review the Beylkin formula and some of the advantages and disadvantages of its use in resolution analysis and survey design. Simple examples for a homogeneous geologic model illustrate the wavenumber and space-domain images and how they depend on simple acquisition geometries. We then apply the approach to a model of a salt dome structure that causes significant ray-bending effects. These results present a significant advance over previous work, which typically considers only relatively simple geologic structures (e.g., von Seggern, 1994; Vermeer, 1999). Because of the complex wave propagation properties, resolution predictions are less intuitive. Furthermore, we compare the resolution for a marine geometry with results for a radial survey geometry based on a joint surface seismic/vertical seismic profiling (VSP) survey recently conducted in the onshore Gulf Coast area and suggest a simple method to assess loss in image quality as the S/N ratio decreases.

METHOD

Background theory

Beylkin et al. (1985) introduce a solution for inverse acoustic wave scattering based on a model where the unknown values of bulk modulus and density are defined as perturbations to a smoothly varying initial model. The scattered waves are described using the Born approximation, and the inverse algorithm applies ray methods to compute the traveltimes and amplitudes of waves traveling from source to image point and back to the receiver. This approach, and similar methods for elastic media, have been described in a number of references (e.g., Beylkin, 1985; Beylkin et al., 1985; Beylkin and Burrige, 1990). The key result for analyses of image resolution is an equation relating the reconstructed estimate of the unknown medium $f_{est}(\mathbf{x})$ to the true structure $f(\mathbf{x})$:

$$f_{est}(\mathbf{x}) = \frac{1}{2\pi^3} \int_{D_x} f(\mathbf{k}) e^{-i\mathbf{k}\cdot\mathbf{x}}. \quad (1)$$

Here, $f(\mathbf{k})$ is the wavenumber domain transform of the subsurface object with nonzero values of perturbation $f(\mathbf{x})$ (mathematical notation is summarized in Table 1). The most important aspect of this transform relationship is the domain of integration D_x , which, unlike conventional Fourier transforms, does not extend to infinity. Instead, this domain is controlled by the source–receiver acquisition geometry. The wavenumber vector \mathbf{k} appearing in equation (1) is

$$\mathbf{k} = \omega \nabla_x [\phi^{sc}(\mathbf{x}, \xi) + \phi^{in}(\mathbf{x}, \eta)], \quad (2)$$

where $\phi^{sc}(\mathbf{x}, \xi)$ and $\phi^{in}(\mathbf{x}, \eta)$ represent traveltimes from a receiver at location ξ to the scatterer at \mathbf{x} and from the source

at η to the scatterer, respectively. The gradients of the traveltime are slowness vectors, which are tangent to the rays at the image points (Figure 1). Therefore, the image wavenumber vector resulting from a specific source–receiver pair is the sum of the slowness vectors along the rays from both source and receiver down to the image point, weighted by frequency. The more restricted the region of the surface occupied by sources and receivers, the more restricted the range of the wavenumber domain covered in this Fourier integral and the worse the reconstruction of the image $f_{est}(\mathbf{x})$.

This approach to inversion and resolution is based on the Born approximation for scattered acoustic waves; in this framework, it is natural to consider the earth model as discretized into individual volume elements that can be modeled as point scatterers. We adopt this viewpoint below.

Calculations of resolution

Equation (1) provides a simple approach for computing a predicted spatial image, given the wavenumber domain representation of the scattering object $f(\mathbf{k})$. One straightforward method for comparing competing survey designs for a given earth model is to compute the image of a point scatterer located at a target region of interest within the model. The reconstructed image will never exactly reproduce the point object

Table 1. Nomenclature.

Symbol	Definition
$f(\mathbf{k})$	Fourier transform of subsurface scattering object (wavenumber domain)
$f_{est}(\mathbf{x})$	Reconstruction in space domain of subsurface scattering object
\mathbf{k}	Wavenumber vector
t	Time
\mathbf{x}	Cartesian spatial coordinates
γ	Parameter in definition of source wavelet [equation (3)]
η	Cartesian coordinates of a receiver location
ξ	Cartesian coordinates of a source location
ϕ^{in}	Traveltime from source to scatterer location
ϕ^{sc}	Traveltime from scatterer to receiver location
ω	Angular frequency

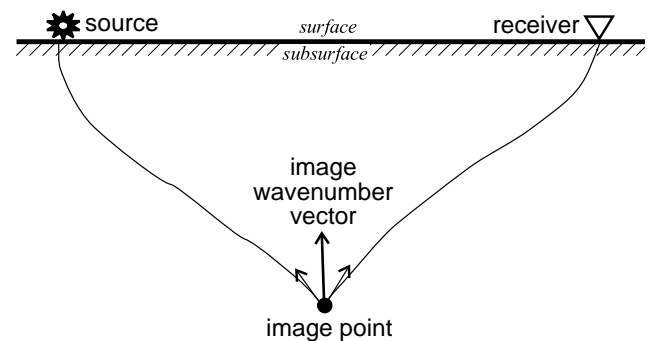


FIG. 1. Schematic of the wavenumber vector described by equation (2). The wavenumber vector that represents the portion of the wavenumber domain resolved by data acquired by the illustrated source–receiver pair is the bold vector, the sum of the two vectors tangent to the raypaths at the image point. The oppositely directed wavenumber vector is also included in the wavenumber domain (Beylkin et al., 1985).

because of the limitations in bandwidth and acquisition geometry, and the size of the resulting image provides a measure of the optimal theoretical image. Alternatively, an examination of the wavenumber domain is useful, since the transform of the point scatterer is a constant value. Any variations in magnitude indicate some reduction in image quality.

Since the desired result is in the space domain, we begin calculations by specifying the extent of the output spatial image in the x -, y -, and z -directions and the spatial discretization interval dx . Standard Fourier relationships provide the corresponding Nyquist wavenumber and wavenumber discretization value dk . For each source–receiver pair, ray tracing must be applied to compute the slowness vectors appearing in equation (1).

The only other complication is applying the source spectrum to accurately reproduce the loss in resolution because of finite bandwidth. For all results in this paper, we use a source wavelet $s(t)$ defined as

$$s(t) = \cos(\omega t) e^{-(\omega t/\gamma)^2}, \quad (3)$$

where $\gamma = 3$ and angular frequency $\omega = 2\pi 30$. As the sum wavenumber vector is computed for each source–receiver pair at frequency ω , its magnitude is scaled by the magnitude of the source spectrum at that frequency.

The resolution results in both the wavenumber domain and the space domain indicate of the best possible migrated image of a point scatterer. Furthermore, this method avoids the time-consuming process of computing and migrating synthetic seismograms and is therefore more cost effective than attempting to simulate a proposed experiment directly. At the same time, the method obviously neglects any uncertainty in the earth model used in the calculations, as well as any errors in imaging velocity models or noise in the data. Therefore, the resolution obtained with field data will always be somewhat worse than predicted. As long as these sources of errors have similar importance throughout the model, the results should still show the correct changes in resolution both laterally and vertically.

RESOLUTION AND ACQUISITION GEOMETRY IN HOMOGENEOUS MEDIA

The resolution analysis is easily illustrated for homogeneous media, where the raypaths are obviously straight lines connecting source or receiver and the image point. While such examples may seem trivial, they provide very important insights that are broadly applicable to acquisition over geologic models with gentle structure where raypath bending is minimal, since small changes in ray directions result in only small perturbations to the wavenumber vectors computed with equation (2).

For example, Figure 3 compares the wavenumber-domain images for a single zero-offset, vertical incidence source–receiver pair and for the surface array shown in Figure 2. The surface array consists of 81 sources and coincident receivers, spaced every 50 m for a total length of 2 km. All shots are fired into all receivers. The rays for the single source–receiver pair are vertical, so the corresponding wavenumber vector is vertical (Figure 3a). On the other hand, the array includes raypaths with a larger aperture, so a much larger portion of the wavenumber domain is illuminated (Figure 3b).

Transforming these images back to the space domain yields the predicted migration images of the point scatterer (Figure 4). The vertical wavenumber vector transforms to a

horizontal, planar image (Figure 4a), while the multioffset experiment produces a comparatively well-resolved image of the point scatterer (Figure 4b). Migrations of synthetic data computed for the multioffset experiment produce an image that is indistinguishable from Figure 4B, confirming the accuracy of the image prediction. On the other hand, the migration of data from the single source–receiver pair will be the well-known half-circle imaging impulse response. The Beylkin formula [equation (1)] yields information only on the Fourier wavenumber domain components that are resolved at a specific image point, so it instead produces the plane-wave component (Figure 3a).

For these simple geometries, the best spatial resolution is theoretically obtained with an array of zero-offset source–receiver pairs, since the slowness vectors for the source and receiver rays coincide and their vector sum will be a maximum (e.g., Vermeer, 1999). When we repeat the calculations for the geometry of the preceding example using only a zero-offset receiver for each of the 81 sources, the resolution improves over the image obtained using a multioffset array (Figure 5). Since the array has exactly the same total length for both cases, the aperture of directions occupied in the wavenumber domain is the same. However, the wavenumber vectors in the zero-offset model are all the same length, and the only reason the amplitudes vary in Figure 5a is because of the binning that occurs in Cartesian coordinates. In practice, the increase in S/N ratio will likely compensate for the degradation in resolution obtained using the idealized model.

SURVEY DESIGN FOR A SALT DOME MODEL

While the preceding results provide general insight into the types of resolution that will be obtained for acquisition in areas with minimal geologic structure, a complete calculation of rays is required for more complex models, and results may be difficult to predict prior to computation. As an example, we consider a model of a salt dome structure (Figure 6). The layers

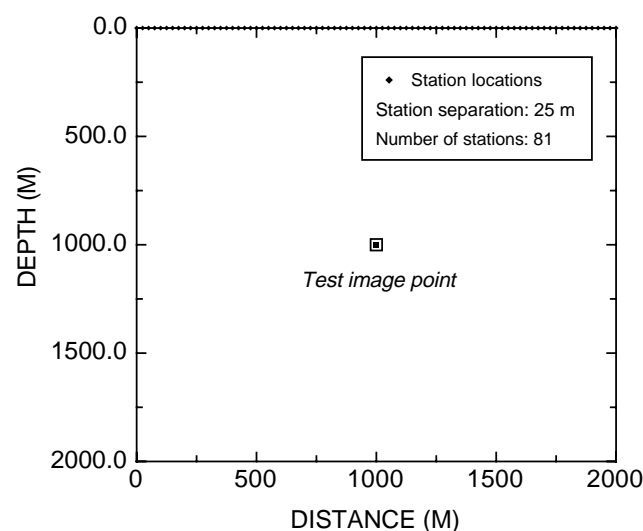


FIG. 2. Acquisition geometry for Figures 3, 4, and 5. The symbols mark station locations at which both sources and receivers were located on the free surface. Sources occupied each station, and active receivers were located at all 81 stations for each shot.

in this model each have a constant velocity with increasing values of 1.7, 2.2, and 3.0 km/s. The salt is also homogeneous, with a higher velocity than the surrounding layers (4.5 km/s). While most of the salt is contained within a tall, cylindrical structure, there is also a thin, horizontal component representing a feeder stock on one side.

To consider the influence of acquisition geometry on imaging near and beneath the salt structure in the model, we consider two very different types of acquisition. The first geometry corresponds to a simple marine experiment with a single towed cable (Figure 7). The total configuration includes 75 parallel lines, with source and receiver in-line spacing of 50 m and cross-line spacing of 150 m. The cable is 3 km long, with 60 receivers to record each shot. The nearest offset receiver is located 50 m from the source. All of the source positions are located in a rectangular area above the salt dome, while receiver

positions naturally extend outside this region since the cable always trails the boat. The geometry of the area occupied by all stations was designed to provide a similar aperture and total number of source–receiver pairs as used in the second geometry, a land acquisition pattern based on a field experiment used for imaging a salt structure in the Gulf of Mexico region (Constance et al., 1999). This survey geometry included sources located along circles with radii increasing in increments of 330 m, while receivers were located along radially directed lines every 10° . At larger distances from the center of the experiment, additional receiver lines were inserted to maintain uniform data coverage. The shorter infill receiver lines were inserted halfway between the complete lines, creating a spacing of 5° at large offsets. Source spacing was 50 m along the circles, and in-line receiver spacing was also 50 m. During field data recording, receivers within a 90° wedge were active

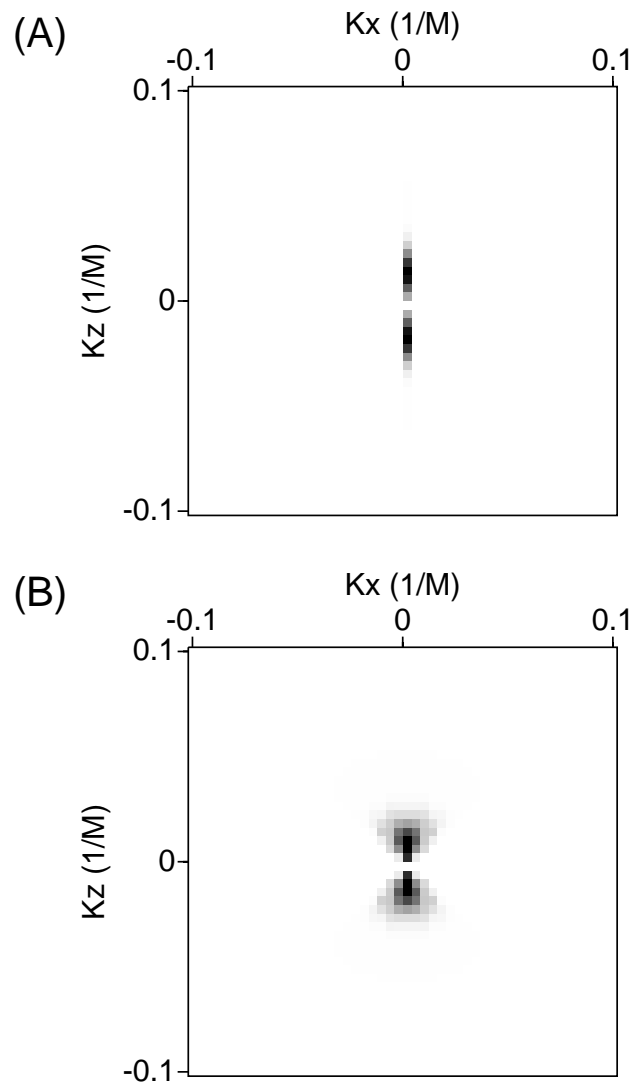


FIG. 3. Wavenumber-domain images of the point scatterer at the test point in Figure 2. (a) Zero-offset result for colocated source and receiver at $(x, z) = (1000, 0)$ in Figure 2. (b) Result obtained using all source and receiver locations in Figure 2.

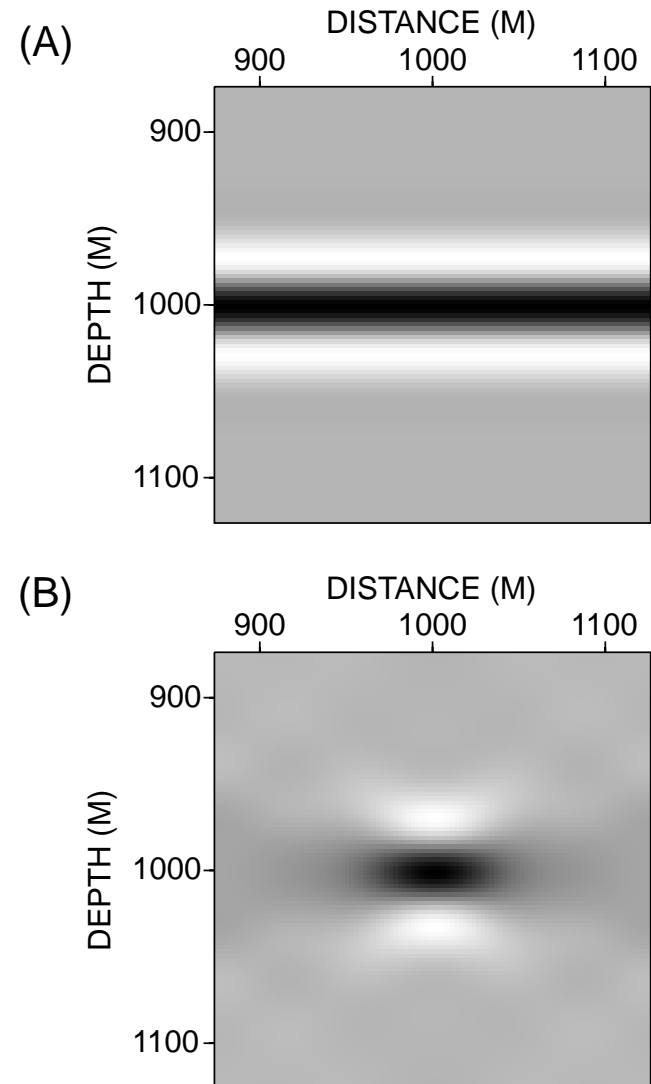


FIG. 4. Space-domain images of the point scatterer at the test point location in Figure 2. Fourier transforms of the wavenumber-domain images in Figure 3. (a) Zero-offset result for colocated source and receiver at $(x, z) = (1000, 0)$ in Figure 2. (b) Result obtained using all source and receiver locations in Figure 2.

when sources located in the center 10° arc of the wedge were detonated.

This geometry is displayed in Figure 8, which shows a decimated set of source positions for clarity. Geometries similar to this have been suggested as effective designs for high-quality imaging near salt structures since they have a symmetry that is similar to that of the hypothetical structure and should provide fairly uniform illumination (e.g., Maldonado and Hussein, 1994). Our calculations therefore test whether this suggestion is correct and also show the potential differences in image quality between the very different land and marine geometries.

Subsalt imaging

The first imaging target we consider is a horizon at a depth of 4 km, which is several hundred meters beneath the salt dome

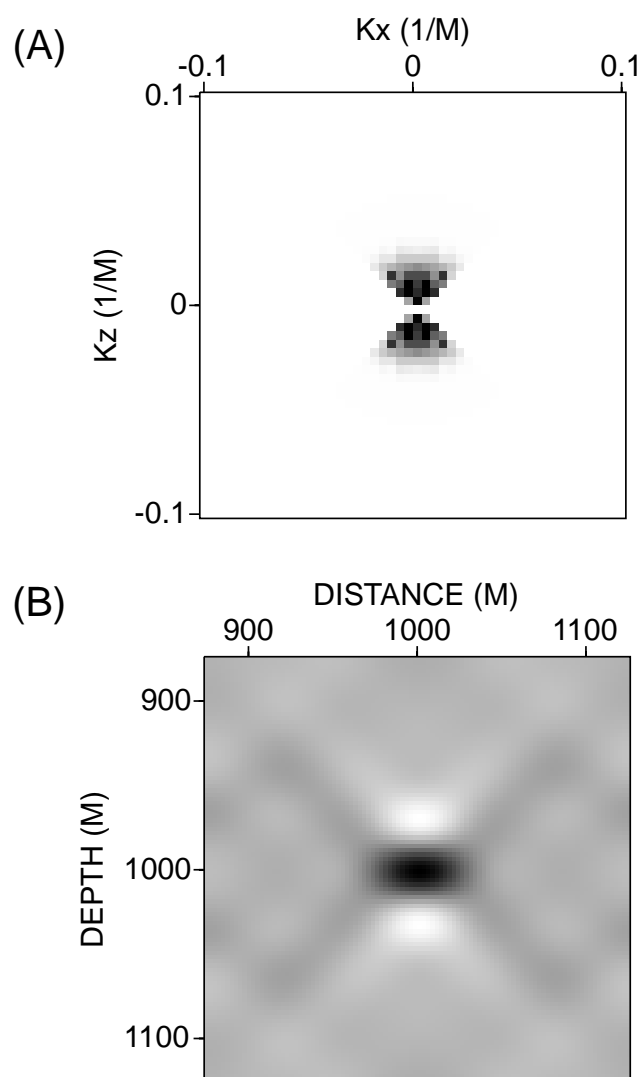


FIG. 5. (a) Wavenumber- and (b) space-domain images of the scatterer at the test point using a zero-offset acquisition geometry. Resolution is better than for the multioffset geometry (Figure 4b). These images are obtained by considering zero-offset source–receiver pairs located at each of the 81 stations in Figure 2.

(Figure 6). Specifically, we consider a grid of image points extending over a rectangular region from $x = 7$ to $x = 10$ and from $y = 6$ to $y = 11$, with point scatterers located at intervals of 0.3 km. A perfect image would produce a single pixel at each location, but the acquisition geometries and band-limited data instead yield smeared images with different degrees of resolution (Figure 9). To minimize computation time, we considered only single-offset imaging, the near- and far-offset source–receiver pairs for the marine geometry (50 and 3000 m, respectively), and the nearest-offset receiver for the land geometry (ranging from 0 to 275 m). In the land case, it is straightforward to find the receiver that is closest to each source station, but there is no obvious way to choose the far-offset trace given the large wedges of receivers that are active for each source event. Although it would be possible to arbitrarily select the largest possible source–receiver distance, in practice there would be no logical pattern to the azimuthal offset of the receiver in this case, so we did not attempt to follow this approach.

These single-offset results let us make some important conclusions. First, unlike the idealized homogeneous model with the simple acquisition geometry considered above (Figures 2, 4, and 5), the marine experiment provides better resolution for the far offsets, not the near offsets. This result can be explained by considering the ray geometries (Figure 10). The large-offset rays correspond to a much larger aperture at the subsalt image points, and the aperture in the wavenumber domain is also larger, producing better spatial resolution.

The single-offset calculations also allow some predictions of resolution in multioffset migration. Since a final image produced from all offsets would essentially be an average of the results of single-offset imaging, we can infer that the result for the marine acquisition geometry would lie somewhere between the results for the images shown in Figures 9a and 9b. Since the near-offset land geometry clearly produces better resolution (Figure 9c), we can infer that it should in fact provide a better resolved subsalt image even if resolution is somewhat worse at larger offsets. This suggests that the more complicated land geometry can be very effective.

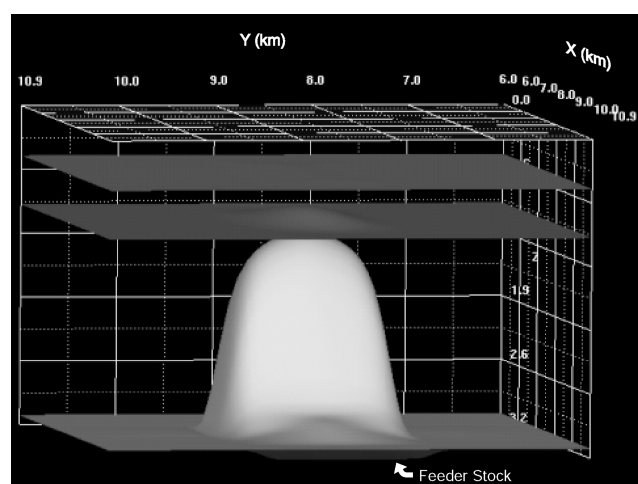


FIG. 6. Perspective view of the salt model used for testing survey design. A small, thin feeder stock can be observed near the center of the model on the front side of the image. The salt thickness is negligible outside of the dome and the feeder stock.

Another very important point is that a conventional illumination study simply counting the number of rays striking different regions of the subsalt image surface indicates that the total number of rays does not decrease significantly in the low-resolution central region of the surface. Instead, the loss in resolution occurs because ray bending causes the largest fraction of the rays to travel in near-vertical directions. Since the corresponding wavenumber vectors will be oriented in the vertical direction as well, the horizontal resolution decreases significantly. This demonstrates why simple illumination analyses may be misleading in terms of understanding spatial resolution, although they may provide other insights.

Salt flank imaging

The resolution predictions clearly indicate the land geometry will yield better resolved images than the marine geometry for the subsalt target. However, the more important exploration target might be in formations adjacent to the salt dome. Figure 11 shows the locations of four such test locations—A, B, C, and D—all at a depth of 2 km.

Unlike the subsalt case, the near-offset imaging with the marine acquisition geometry yields somewhat better resolution than the far-offset images, though the differences are not as obvious (Figures 12, and 13). On the other hand, the resolution of these point scatterers with the land geometry is just as good as that obtained with the near-offset marine configuration for points C and D (Figures 14c and 14d) but is noticeably

better for points A and B (Figures 14a and 14b). The land survey design more consistently and uniformly illuminates the image points, while the towed-cable geometry involves a larger concentration of raypaths near the y - z plane. Therefore, the land geometry should provide a more robust and reliable imaging result for this salt structure.

The circular/radial land geometry and the simple marine geometry present a rather extreme contrast in designs. To better compare competing land geometries, we also examined an orthogonal land survey geometry that matched the aperture and total number of source-receiver pair criteria of the two previously mentioned geometries. It consisted of 34 source and 34 receiver lines, orthogonal to each other. The source and receiver line intervals were 360 m, with sources and receivers spaced every 60 m. All sources were recorded into receiver patches that were 100 receivers by 16 receiver lines. The aspect ratio of each line receiver patch was 84%, providing a wide azimuth distribution. After careful examination of its effects on imaging, we found that the orthogonal geometry yielded results that are very similar to the circular land geometry for both the subsalt and the salt flank targets. The important point is that both the circular and the orthogonal land geometries result in a fairly smooth azimuthal angle distribution of rays arriving at image points. On the other hand, the marine geometry, with its single towed cable, has an inferior coverage of ray directions, producing worse spatial resolution.

Resolution and S/N ratio

All of the results presented to this point assume perfect imaging and a well-constrained model. At least some of these

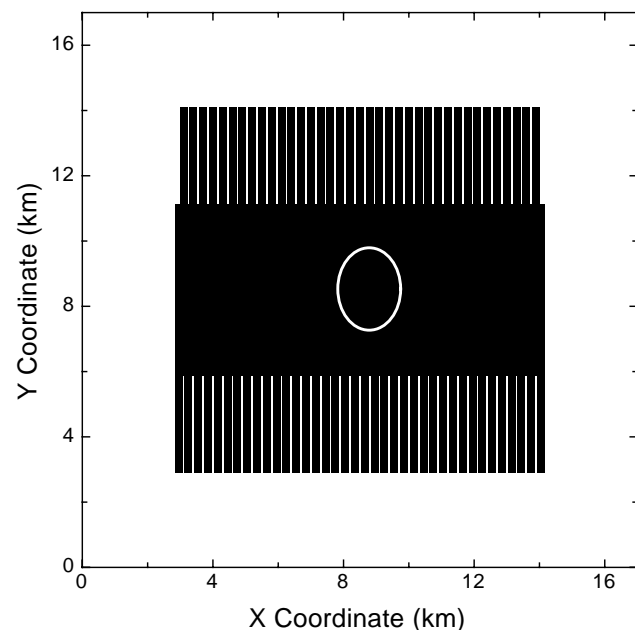


FIG. 7. Marine acquisition geometry used to compute image resolution for the salt dome model (Figure 6). The elliptical outline in the center indicates the approximate location and shape of the salt structure beneath the experiment. The station locations correspond to a single-cable geometry. The hypothetical ship sailed in the vertical direction, firing in the region from $y = 6$ to $y = 11$ km. Since the receivers are towed behind the boat and the boat sailed alternately up and down, there are stations outside of the total source region.

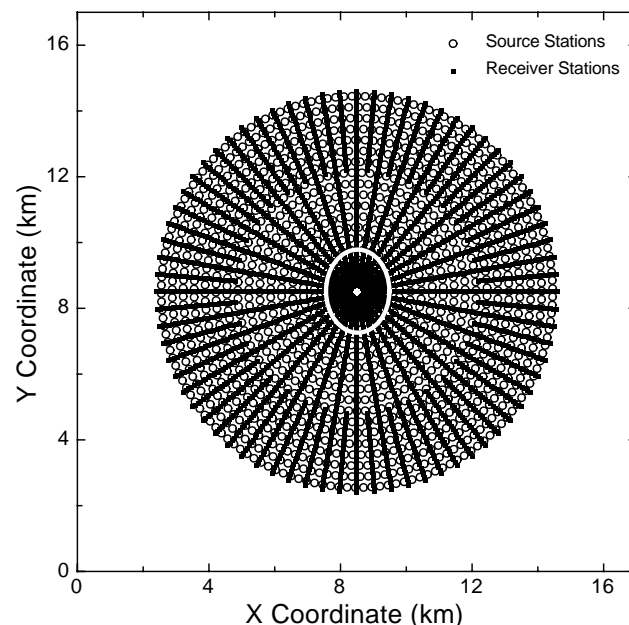


FIG. 8. Land acquisition geometry used to compute image resolution for the salt dome model (Figure 6). The elliptical outline in the center indicates the approximate location and shape of the salt structure beneath the experiment. This geometry is based on that used in the field experiment described by Constance et al. (1999). This figure shows only the locations of every fifth source along the concentric source line circles for clarity.

constraints, however, can be relaxed in a realistic manner. For example, by computing ray amplitudes as well as ray trajectories, the influence of decreasing S/N ratios can be considered. If A_0 is the largest diffracted amplitude recorded by the experiment, then we can consider it to be a measure of the signal strength and define the noise level relative to it. For an S/N ratio of 4, for example, we assume that a ray with an amplitude less than $A_0/4$ will not contribute to the imaging and we neglect its contribution to the spatial resolution calculation. This approach is not strictly correct, since the stacking procedure will tend to suppress noise during imaging, and signals weaker

than noise might still contribute effectively to the final image. Because of the simplicity of this approach, we also do not attempt to account for any \sqrt{n} factor resulting from summing over traces. However, this does allow a simple way of quantitatively filtering out weaker contributions to the image and allows a straightforward analysis of how decreasing S/N ratios might reduce spatial resolution.

Application of this procedure to the salt flank images point A illustrates such a degradation in images quality (Figure 15). As the S/N ratio decreases from ∞ to four, the images lose resolution, especially for the far-offset marine geometry at the lowest S/N ratio. In this case, it becomes clear that though the very large offsets effectively increase imaging aperture, the corresponding weak signals may be difficult to use in practical cases. Also, the land acquisition geometry is still more robust in that the image quality shows comparatively little reduction in resolution for this range of S/N ratios, though it will eventually start to decrease for lower ratio values.

DISCUSSION AND CONCLUSIONS

The Beylkin formula [equation (1)] provides an important tool for analyzing variations in spatial resolution on seismic images. Since it uses only ray geometry to predict image distortion, computing hypothetical point scatterer images rapidly is

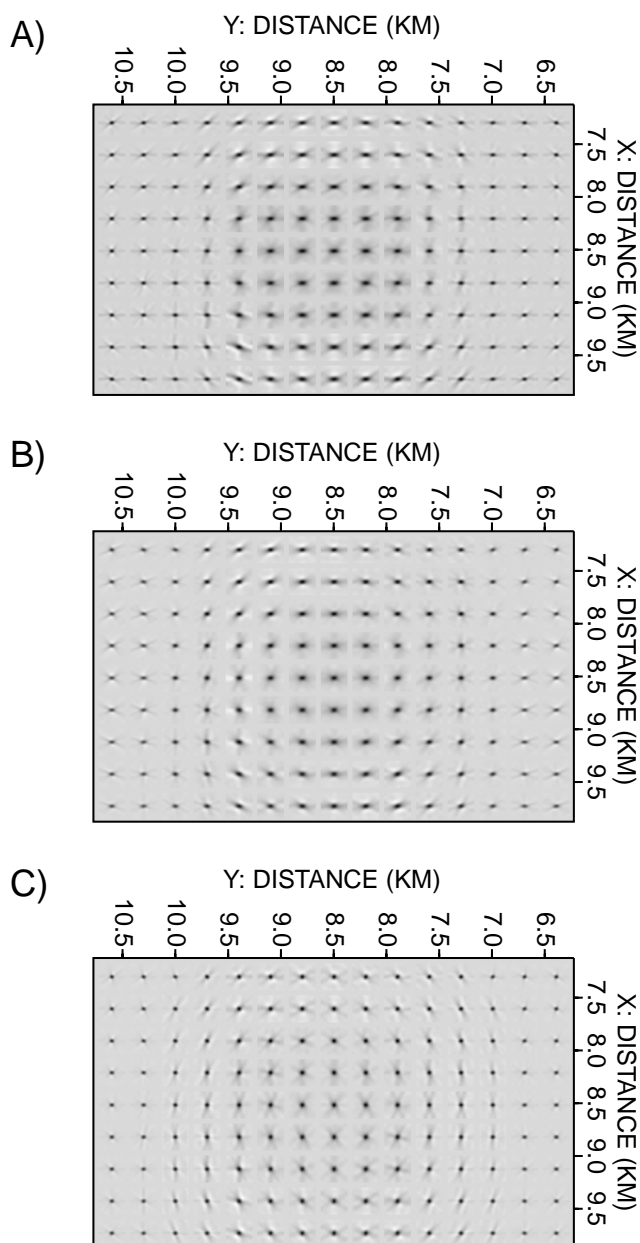


FIG. 9. Subsalt resolution obtained using the acquisition geometries in Figures 7 and 8. Each figure shows the point scatterer images predicted for a depth of 4 km in a region underlying the center of the salt dome. (a) Near offsets, marine acquisition geometry. (b) Far offsets, marine acquisition geometry. (c) Near offsets, land acquisition geometry.

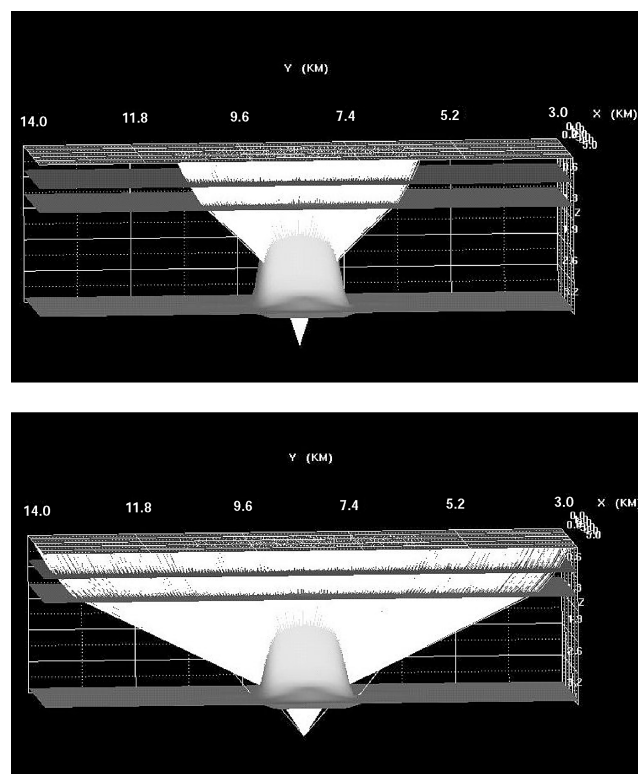


FIG. 10. Comparison of raypaths for near- (above) and far-offset (below) pairs in the marine acquisition geometry (Figure 7) for the point beneath the center of the salt dome. Only rays for several lines near the center of the survey are displayed for clarity. The predicted image resolution is better for the far-offset geometry because the wavenumber vectors will include a larger aperture, as shown by the correspondingly larger ray aperture at the image point.

relatively straightforward, especially compared to a sequence of forward modeling followed by migration. The results are also broadly applicable to a range of acquisition geometries, and converted wave imaging can be examined. Our examples for simple geometries illustrate this approach and show how resolution depends on the size of an array. Furthermore, since zero-offset source–receiver rays are coincident, the longest image wavenumber vectors and best image resolution are obtained with near offsets for the simple acquisition geometries.

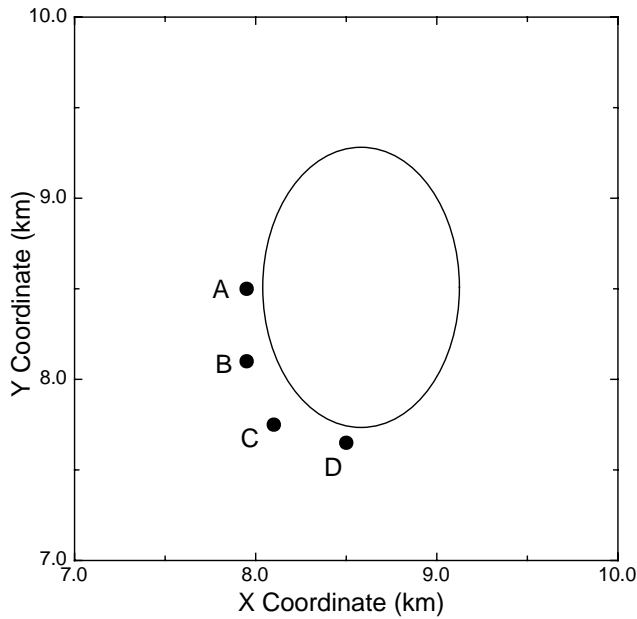


FIG. 11. Locations of four points located near the salt dome at a depth of 2 km. These points are used to assess the salt flank imaging potential of the marine and land acquisition geometries (Figures 7 and 8).

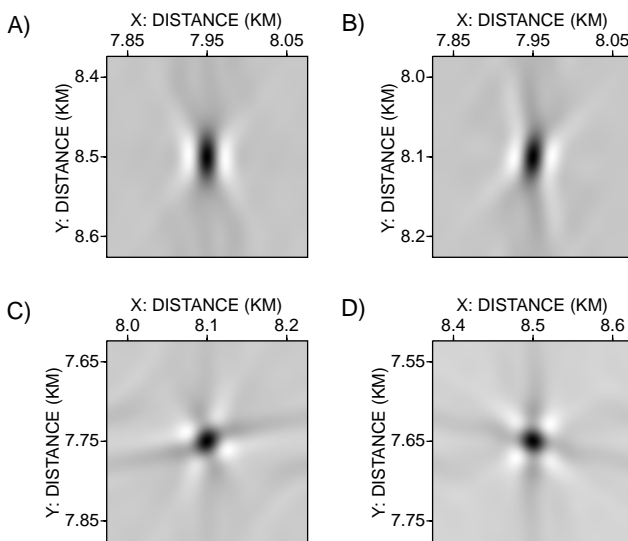


FIG. 12. Spatial resolution for the four salt flank image points in Figure 11, using the near offsets from the marine acquisition geometry.

The comparison of land and marine survey geometries shows the value of directly considering image resolution when comparing competing designs for the more realistic, complex geometry of a salt dome structure. One point that becomes clear is that for regions with significant structural complexity associated with strong ray bending and more realistic acquisition geometries, near-offset images do not necessarily provide the best spatial resolution. The single-cable marine geometry produces better resolution for the large-offset source–receiver pairs, both because it includes rays traveling closer to horizontal and because the far-offset receivers extend a significant distance outside the region containing the shot locations. Furthermore, the number of ray reflection points is still fairly high for the near-offset experiment, emphasizing that such fold

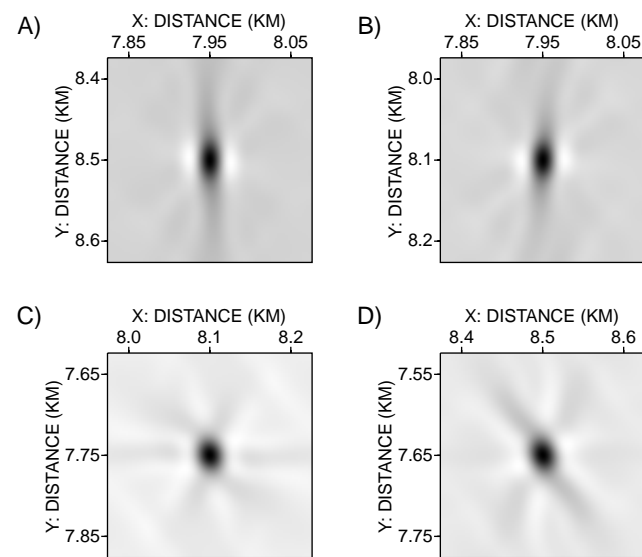


FIG. 13. Spatial resolution for the four salt flank image points in Figure 11, using the far offsets from the marine acquisition geometry.

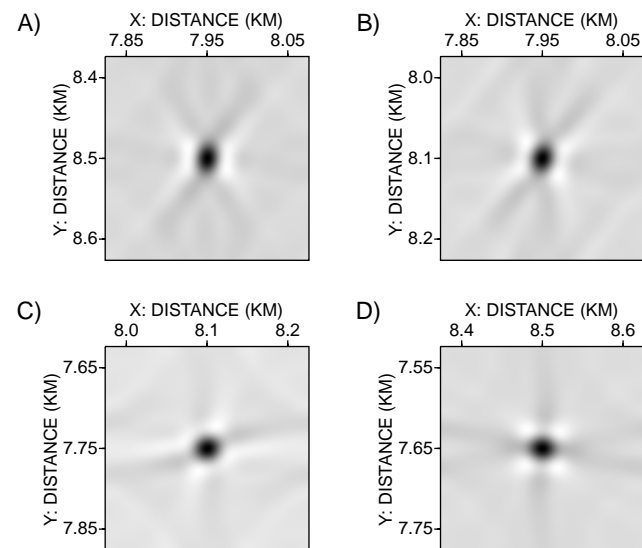


FIG. 14. Spatial resolution for the four salt flank image points in Figure 11, using the near offsets from the land acquisition geometry.

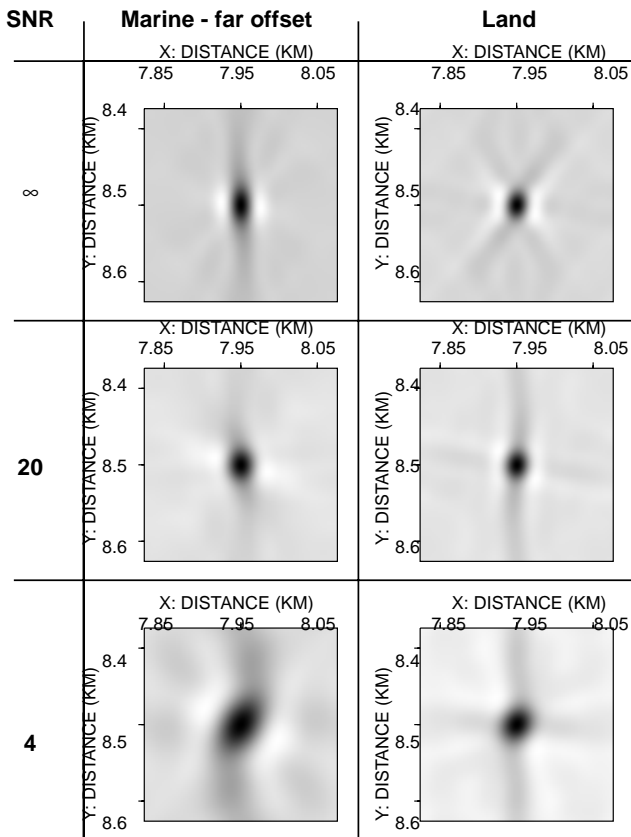


FIG. 15. Spatial resolution for the salt flank image point A from Figure 11 for different S/N ratios (SNR). The left column displays results for the far offsets from the marine geometry; the right column is for the near offsets from the land survey. The uppermost pair of figures shows the results for perfect, noise-free data, identical to the corresponding images in Figures 13 and 14.

measurements would be misleading when estimating image resolution. Resolution predictions for the land survey, with its concentric rings of sources, help to confirm that this survey may help to improve image quality. This contradicts some previous suggestions that image resolution may not be too sensitive to acquisition geometry (von Seggern, 1994). Most likely, similar conclusions would be made from a comparison of our concentric land geometry with any other relatively narrow swath acquisition geometry like the single-cable towed array.

The computations are based on a very idealized model which assumes that a migration has a perfect velocity model and noise-free seismic data. In general, any predictions must be considered an optimal, best case estimate of the spatial resolution that could be obtained in practice. However, we also

suggest a simple procedure allowing a straightforward assessment of the effects of varying S/N ratio to predict decreasing resolution with degradation in data quality. It is also important to realize that the predictions depend on the ray-tracing algorithm used, at least for complex media leading to multiple arrivals. Since a specific ray tracer may make an arbitrary choice of arrival, or, for example, may arbitrarily choose the first arrival, a different ray geometry and wavenumber resolution vector may be computed. We will consider these effects in future work.

ACKNOWLEDGMENTS

This research was funded by the Gas Research Institute under contract 5096-210-3781 under the guidance of Iraj Salehi. We thank Eugene Lavelly for suggesting many of the ideas that appear in this paper and Bud Pope and Rus Kappius for encouragement and suggestions. Comments by associate editor Steve Roche and Warren Neff helped clarify and improve the text. The FFT calculations for this work are done using the modern and highly optimized routines developed by Frigo and Johnson (1998; see also Frigo, 1999).

REFERENCES

- Beylkin, G., 1984, The inversion problem and applications of the generalized Radon transform: *Comm. Pure Appl. Math.*, **37**, 579–599.
- , 1985, Imaging of discontinuities in the inverse scattering problem by inversion of a causal generalized Radon transform: *J. Math. Phys.*, **26**, 99–108.
- Beylkin, G., and Burridge, R., 1990, Linearized inverse scattering problems in acoustics and elasticity: *Wave Motion*, **12**, 15–52.
- Beylkin, G., Oristaglio, M., and Miller, D., 1985, Spatial resolution of migration algorithms, in Berkhout, A. J., Ridder, J., and van der Wall, L. F., Eds., *Acoustical imaging 14*: Plenum Press, 155–167.
- Constance, P. E., Holland, M. B., and Roche, S. L., 1999, Simultaneous acquisition of 3-D surface seismic data and 3-C, 3-D VSP data: 69th Ann. Internat. Mtg., Soc. Expl. Geophys., Expanded Abstracts, 104–107.
- Frigo, M., 1999, A fast Fourier transform compiler: *ACM SIGPLAN Notices*, **34**, 169–180.
- Frigo, M., and Johnson, S., 1998, FFTW: An adaptive software architecture for the FFT: *Conf. on Acoust., Speech and Signal Proc.*, IEEE, 1381–1384.
- Maldonado, B., and Hussein, S. H., 1994, A comparative study between a rectilinear 3-D seismic survey and a concentric-circle 3-D seismic survey: 64th Ann. Internat. Mtg., Soc. Expl. Geophys., Expanded Abstracts, 921–925.
- Miller, D., Oristaglio, M., and Beylkin, G., 1989, A new slant on seismic imaging: Migration and integral geometry: *Geophysics*, **52**, 943–964.
- Slawson, S. E., Grove, K. D., and Fisher, G. W., 1994, Model-based 3-D seismic acquisition design: 64th Ann. Internat. Mtg., Soc. Expl. Geophys., Expanded Abstracts, 919–920.
- Slawson, S. E., Grove, K. D., and Monk, D. J., 1995, Model-based 3-D seismic survey design: 57th Ann. Internat. Mtg., Euro. Assn. Geosci. Eng., Expanded Abstracts, B009.
- Vermeer, G., 1999, Factors affecting spatial resolution: *Geophysics*, **64**, 942–953.
- von Seggern, D., 1991, Spatial resolution of acoustic imaging with the Born approximation: *Geophysics*, **56**, 1185–1201.
- , 1994, Depth-imaging resolution of 3-D seismic recording patterns: *Geophysics*, **59**, 564–576.